Supporting Information

Enhanced photocatalytic CO_2 reduction to CH_4 *via* restorable surface plasmon and Pd_n-$W^{\delta+}$ synergetic sites

Weisheng Hu,[a,‡] Zehua Liu,[c,‡] Liang Chen,*[b] Ting Wang,[a] Yangguang Hu,[c] Ran Long,[c] Dong Liu,*[c,d] Benxia Li*[a]

[a] *School of Chemistry and Chemical Engineering, Key Laboratory of Surface & Interface Science of Polymer Materials of Zhejiang Province, Zhejiang Sci-Tech University, Hangzhou 310018, P. R. China. *E-mail address: libx@zstu.edu.cn (B.X. Li)*

[b] *College of Material, Chemistry and Chemical Engineering, Key Laboratory of Organosilicon Chemistry and Material Technology, Ministry of Education, Hangzhou Normal University, Hangzhou 311121, P. R. China. *E-mail address: liang_chen@hznu.edu.cn (L. Chen)*

[c] *Key Laboratory of Precision and Intelligent Chemistry, School of Chemistry and Materials Science, National Synchrotron Radiation Laboratory, School of Nuclear Science and Technology, University of Science and Technology of China, Hefei, Anhui 230026, China. *E-mail address: dongliu@ustc.edu.cn (D. Liu)*

[d] *Sustainable Energy and Environmental Materials Innovation Center, Nano Science and Technology Institute, Suzhou Institute for Advanced Research, University of Science and Technology of China, Suzhou, Jiangsu 215123, China.*

Author Contributions.

‡ Weisheng Hu and Zehua Liu. contributed equally to this work.

1. Supplementary Experiments

1.1 Characterization

X-ray diffraction (XRD) patterns of the catalysts were measured on an X-ray diffractometer (XRD, DX-2700) with monochromatized Cu Kα radiation (λ = 1.5406 Å). Scanning electron microscopy (SEM) imaging was performed on a ZEISS Ultra-55 field-emission scanning electron microscope at an acceleration voltage of 3 kV. Transmission electron microscopy (TEM) imaging and energy dispersive X-ray (EDX) element mapping were performed on a JEOL-2100 transmission electron microscope at an acceleration voltage of 200 kV. X-ray photoelectron spectroscopy (XPS) analysis was performed on an X-ray photoelectron spectrometer (Thermo Fisher Scientific K-Alpha) by using monochromated Al Kα radiation (1486.6 eV) and a high-resolution pass energy of 30 eV with a spot size of 400 μm. The spectra were calibrated according to the C 1s peak of adventitious carbon species at 284.8 eV. The electron spin resonance (ESR) was measured on a Bruker model JEOL JES-FA200 spectrometer. UV-vis-NIR diffused reflectance absorption spectra (DRS) were recorded on a Hitachi UH4150 spectrophotometer. Both CO_2 adsorption (273 K) and N_2 adsorption-desorption isotherms (77 K) were measured on a physisorption apparatus of Micromeritics ASAP 2020. Inductively coupled plasma optical emission spectroscopy (ICP-OES) analysis was conducted on the Agilent 5800 instrument.

1.2 Computational method

Density functional theory (DFT) calculations were carried out using Vienna ab-initio Simulation Package (VASP). The interaction between core and valence electrons was described employing the Projected Augmented Wave (PAW) method. The electron exchange and correlation effects were addressed using the Perdew-Burke-Ernzerhof (PBE) functional form based on the generalized-gradient approximation (GGA). A 2×2×1 Monkhorst-Pack grid of size was employed for the calculations. An energy cutoff of 400 eV for the plane-wave basis was set to ensure the precision. All slab models were applied with 20 Å vacuum layer to avoid the vertical interactions. DFT-D3 method was applied to consider the long-range van der Waals interaction for the adsorption over substrate. The atomic positions were extensively relaxed until the remaining force of each atom is less than 0.05 eV/Å. The binding energy between the adsorbate (ad) and the substrate (sub) is defined by $E_{binding}=E_{ad@Sub}-E_{sub}-E_{ad}$, where $E_{ad@sub}$ is the total energy of substrate with an adsorbed intermediate, E_{sub} and E_{ad} are the energy of substrate and a single adsorbate in vacuum. DFT calculated energies were corrected into free energies (G) according to $G=E_{DFT}+E_{ZPE}-TS$ (298.15K). E_{DFT} is the electronic energy of each step, E_{ZPE} is the zero-point energy and S is the entropy. Meanwhile, the proton-coupled electron ($H^{+}+e^{-}$) transfer during alkyne reduction was simulated with the computational hydrogen electrode (CHE) model. The transition states were searched by means of the climbing image nudged elastic band (CI-NEB) method by relaxing the remaining force below 0.05 eV/Å. The barrier energy (E_a) was calculated according to $E_a=E_{TS}-E_{IS}$, where E_{TS} and E_{IS} are the total energy of the corresponding initial state (IS) and transition state (TS), respectively. The optimized

configurations, adsorption energies, and differential charge densities of CO_2 and H_2O on $W_{18}O_{49}$ and Pd/$W_{18}O_{49}$, where the isosurface value was set as 0.0005 e $Å^{-3}$ for CO_2 adsorption and 0.001 e $Å^{-3}$ for H_2O adsorption.

1.3 Electrochemical measurements

Electrochemical tests were performed using a three-electrode system on an electrochemical workstation (CHI660E, China). The catalyst-coated fluorine-tin-oxide (FTO) glass, platinum wire and Ag/AgCl electrode served as the photoelectrode, counter electrode, and reference electrode, respectively. The linear sweep voltammetry (LSV) profiles of H_2O oxidation were measured at a scan rate of 10 mV s^{-1} in the Ar-saturated 0.1 M $KHCO_3$ aqueous solution, and the applied bias voltage was set in the range of 0 – 2.3 V (vs. Ag/AgCl). The LSV profiles of CO_2 reduction were measured at a scan rate of 10 mV s^{-1} in the CO_2-saturated 0.1 M $KHCO_3$ aqueous solution, with the applied bias voltage ranging from –2.3 to 0 V (vs. Ag/AgCl). The Mott-Schottky plots were recorded at the frequencies of 500, 1000, and 1500 Hz, respectively, with the potential ranging from -2.0 to 2.0 V. The tests were conducted in a 0.1 M Na_2SO_4 solution electrolyte, using a three-electrode system.

1.4 Detection of H_2O_2 generated in photocatalytic CO_2 reduction system

Hydrogen peroxide (H_2O_2) generated in the photocatalytic CO_2 reduction process was analyzed by an iodimetry method. After the photocatalytic reaction, the catalyst was dispersed into 2 mL of deionized water, followed by centrifugation and filtration through a syringe filter. The filtrate was added into a mixture of potassium hydrogen phthalate ($C_8H_5KO_4$) aqueous solution (1 mL, 0.1 M) and potassium iodide (KI)

aqueous solution (1 mL, 0.4 M), where H_2O_2 could react with I^- ions to produce I^{3-} that has a characteristic absorption peak at 350 nm. The UV-vis absorption spectra of the solution were recorded in the wavelength range of 300-500 nm by a Shimadzu UV-2600 spectrophotometer, to quantify the generated H_2O_2.

2. Supplementary Figures

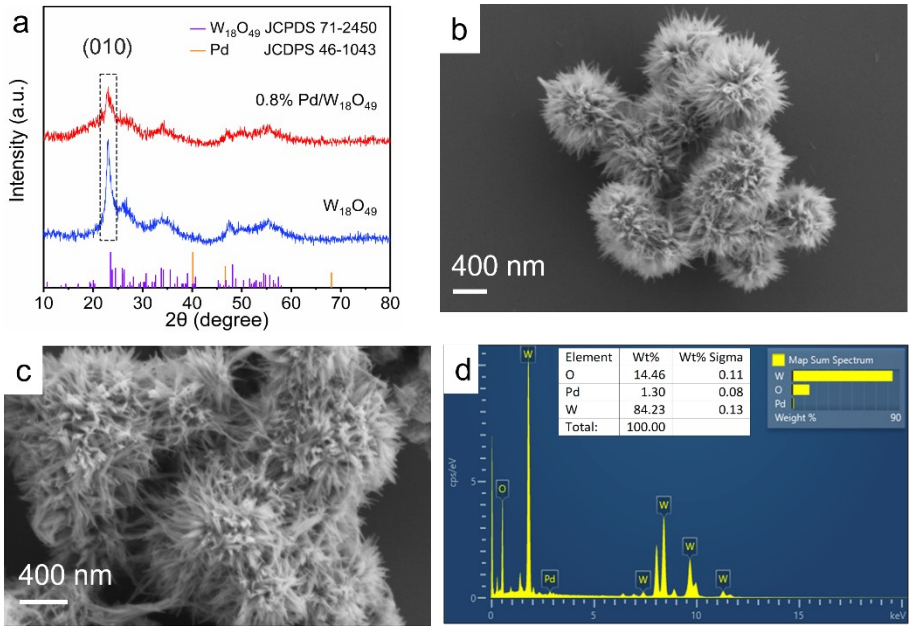

Fig. S1. (a) XRD patterns of $W_{18}O_{49}$ and Pd/$W_{18}O_{49}$, (b) SEM image of $W_{18}O_{49}$, (c) SEM image of Pd/$W_{18}O_{49}$, (d) energy dispersive spectrum of Pd/$W_{18}O_{49}$.

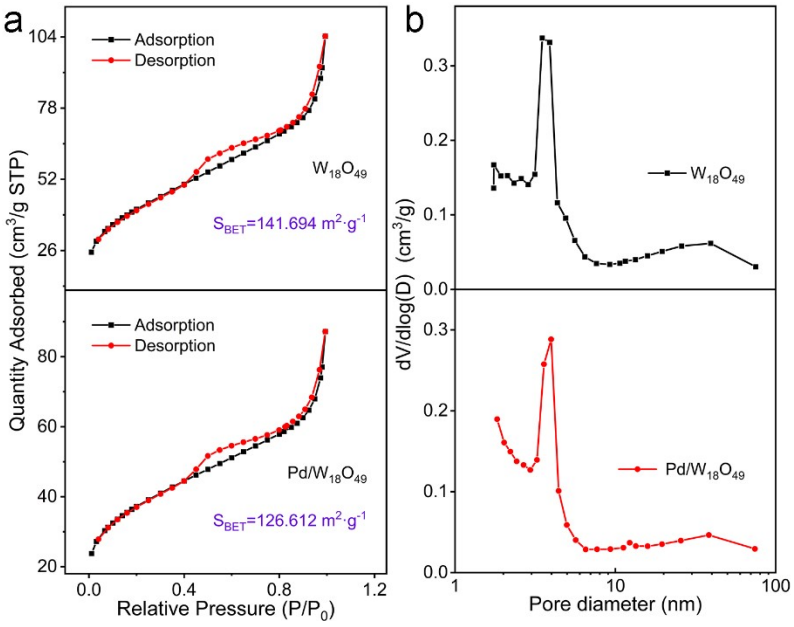

Fig. S2. (a) N_2 adsorption-desorption isotherms and (b) pore size distribution plots of $W_{18}O_{49}$ and $Pd/W_{18}O_{49}$.

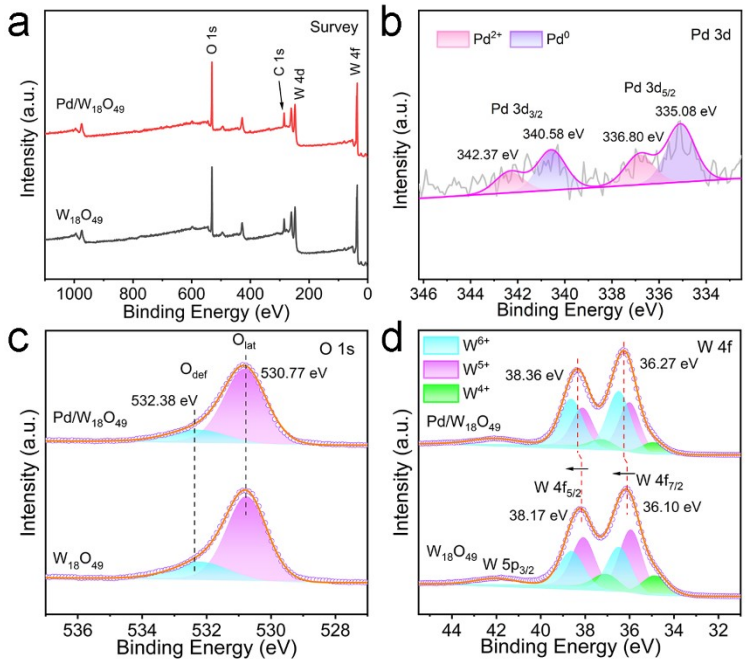

Fig. S3. XPS spectra of $W_{18}O_{49}$ and pristine $Pd/W_{18}O_{49}$. (a) Survey spectra, (b) Pd 3d spectrum of $Pd/W_{18}O_{49}$, (c) O 1s and (d) W 4f spectra.

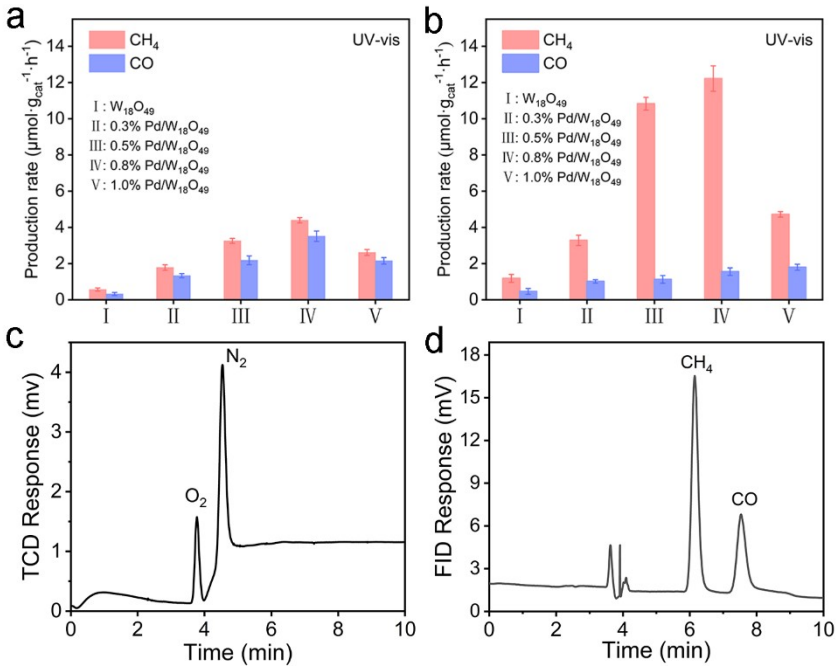

Fig. S4. Results of the UV-vis driven photocatalytic CO_2 reduction using the x%Pd/$W_{18}O_{49}$ catalysts with different Pd contents: (a) without the preactivation process, (b) after the Ar+H_2O preactivation process; (c) TCD-detected GC spectra and (d) FID-detected GC spectra of 1 mL reaction gas extracted from photocatalytic CO_2 reduction system with the Pd/$W_{18}O_{49}$ catalyst after 5 h irradiation.

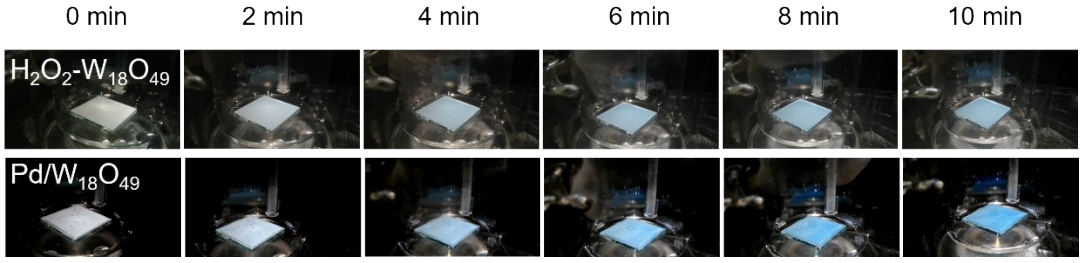

Fig. S5. The color evolutions of H_2O_2-oxidized $W_{18}O_{49}$ and Pd/$W_{18}O_{49}$ in the photoinduced preactivation (Ar + H_2O) process.

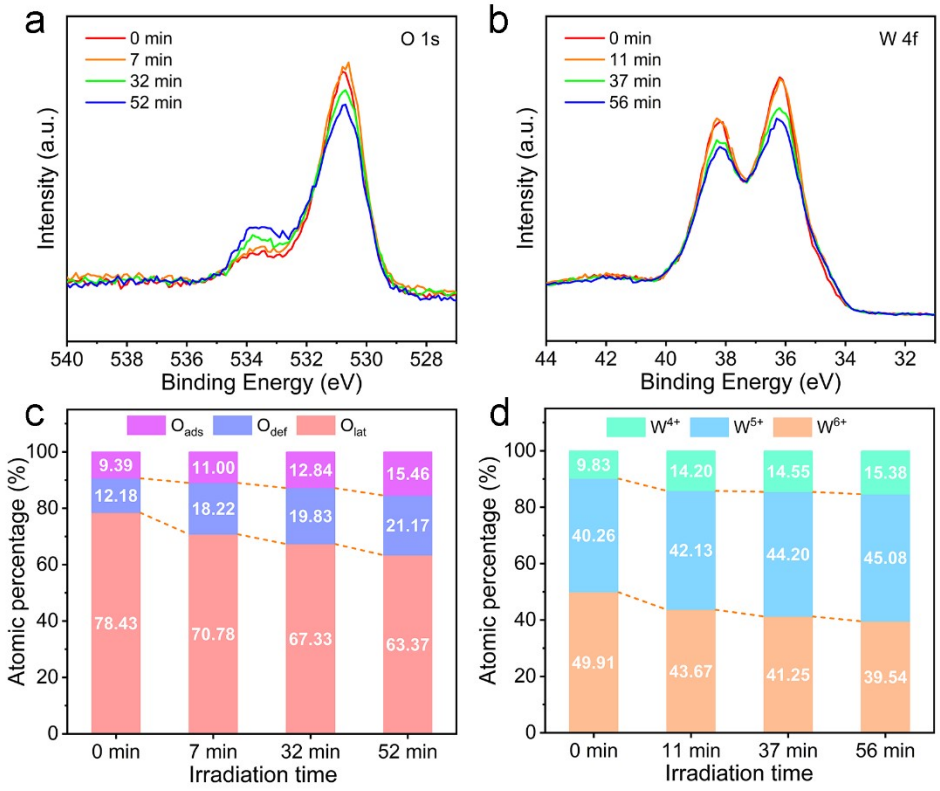

Fig. S6. (a, b) *In situ* NAP-XPS spectra of O 1s and W 4f, and (c, d) the calculated atomic proportions of different O and W species in the Pd/$W_{18}O_{49}$ catalyst during the photoinduced preactivation process.

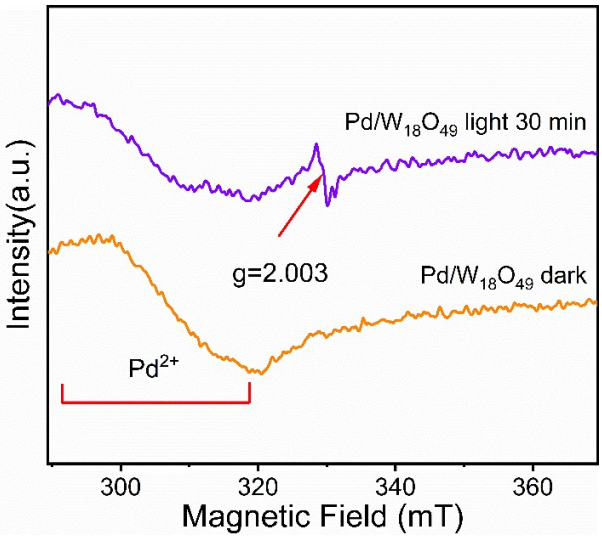

Fig. S7. ESR spectra of the Pd/$W_{18}O_{49}$ sample before and after light irradiation.

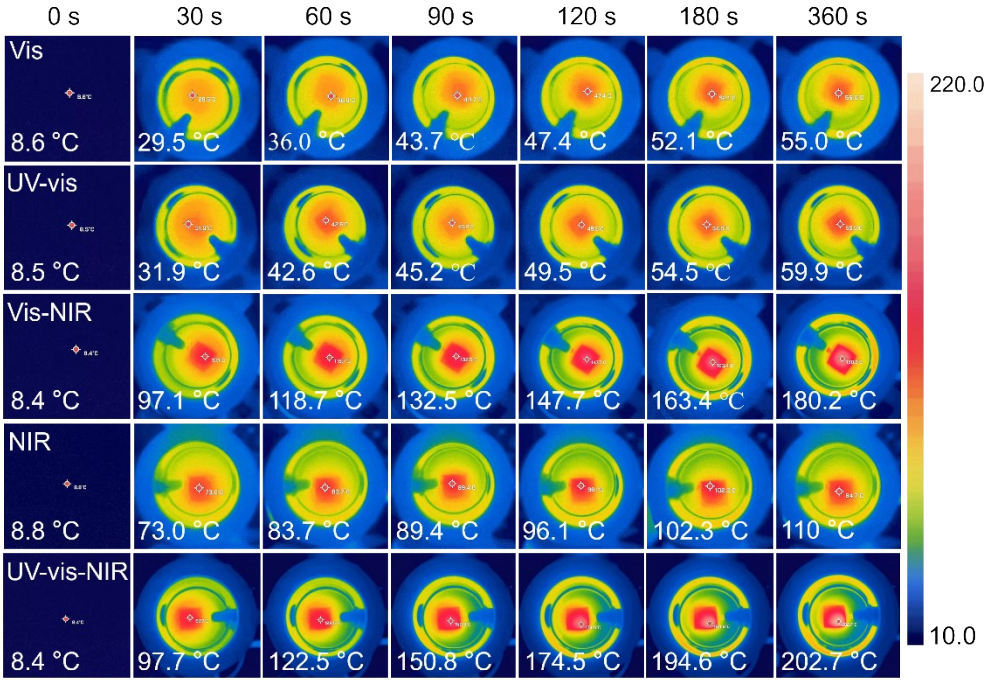

Fig. S8. Time-dependent infrared imagings of the Pd/$W_{18}O_{49}$ catalyst under different light irradiations.

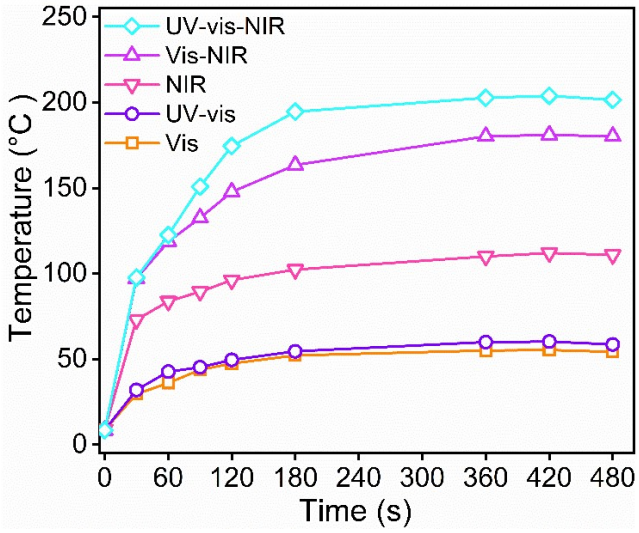

Fig. S9. The temperature profiles of the Pd/$W_{18}O_{49}$ catalyst under different light irradiations for photocatalytic CO_2 reduction.

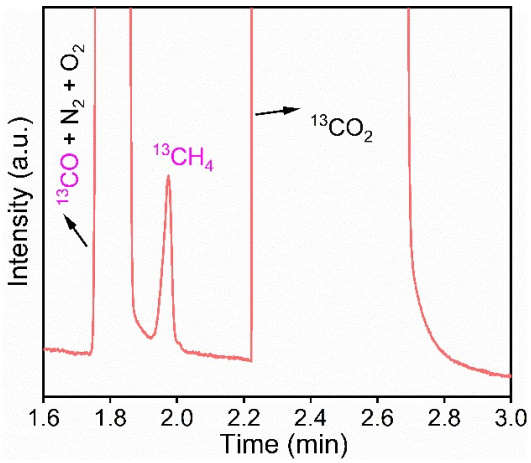

Fig. S10. GC-MS analysis of the CO_2 reduction products from photocatalytic reduction of $^{13}CO_2$ in the presence of $Pd/W_{18}O_{49}$ catalyst.

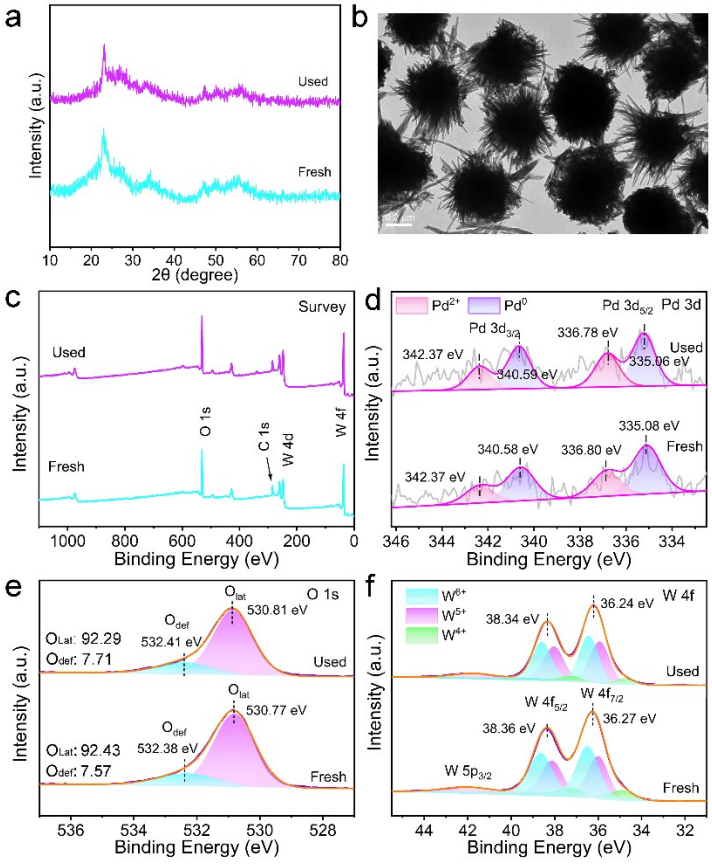

Fig. S11. (a) XRD pattern, (b) TEM image of the $Pd/W_{18}O_{49}$ catalyst after the cyclic CO_2 reduction reaction; (c-f) XPS spectra of the $Pd/W_{18}O_{49}$ catalyst before and after the cyclic CO_2 reduction reaction.

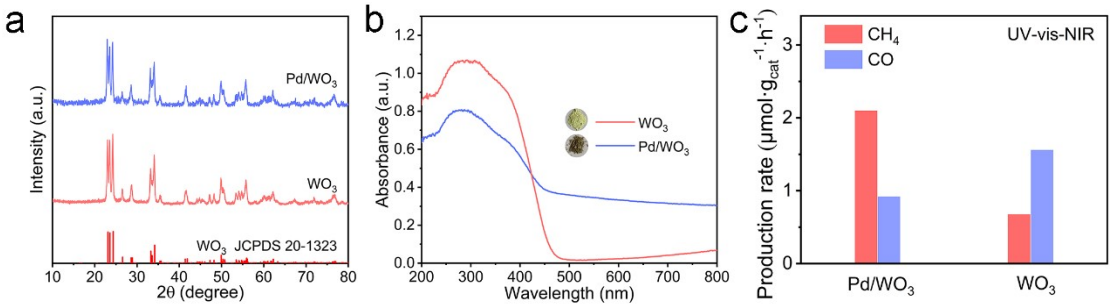

Fig. S12. (a) XRD pattern, (b) UV-vis absorption spectra, and (c) photocatalytic CO_2 reduction performance of the WO_3, Pd/WO_3 samples under UV-vis-NIR illumination.

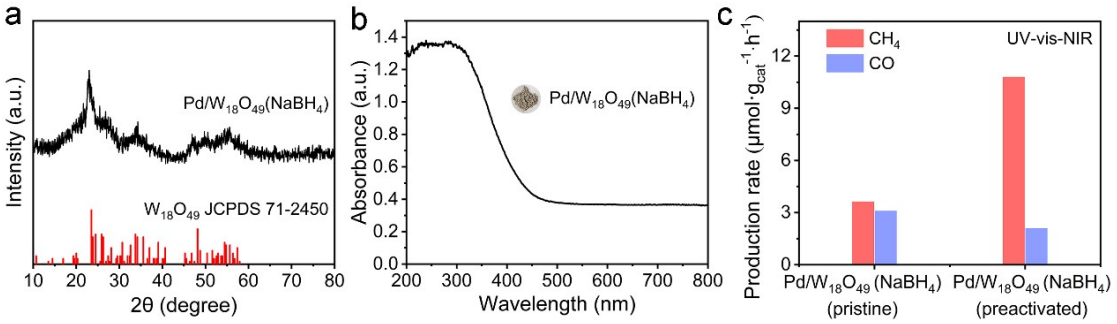

Fig. S13. (a) XRD pattern and (b) UV-vis absorption spectra of the pristine $Pd/W_{18}O_{49}(NaBH_4)$ catalyst, (c) photocatalytic CO_2 reduction performance of the $Pd/W_{18}O_{49}(NaBH_4)$ catalyst under UV-vis-NIR illumination without and with preactivation.

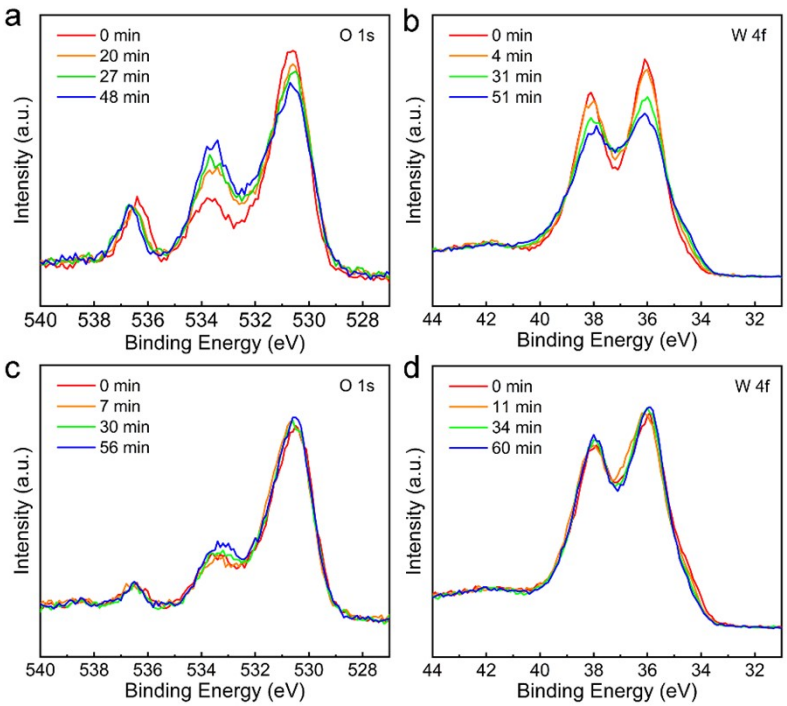

Fig. S14. *In situ* NAP-XPS spectra of O 1s and W 4f of (a-b) the pristine Pd/$W_{18}O_{49}$ catalyst and (c-d) the preactivated Pd/$W_{18}O_{49}$ catalyst in photocatalytic CO_2 reduction process (1.0 mbar CO_2+H_2O).

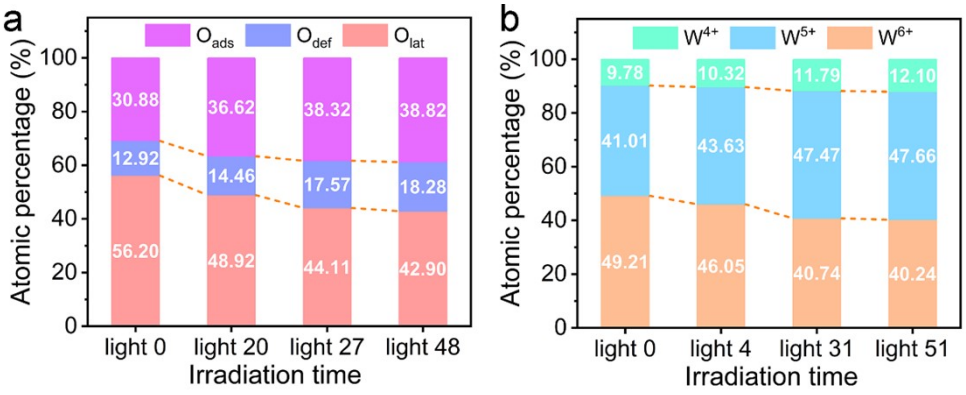

Fig. S15. Atomic proportions of different O and W species calculated from the O 1s and W 4f XPS spectra of the pristine Pd/$W_{18}O_{49}$ catalyst in photocatalytic CO_2 reduction process (1.0 mbar CO_2+H_2O).

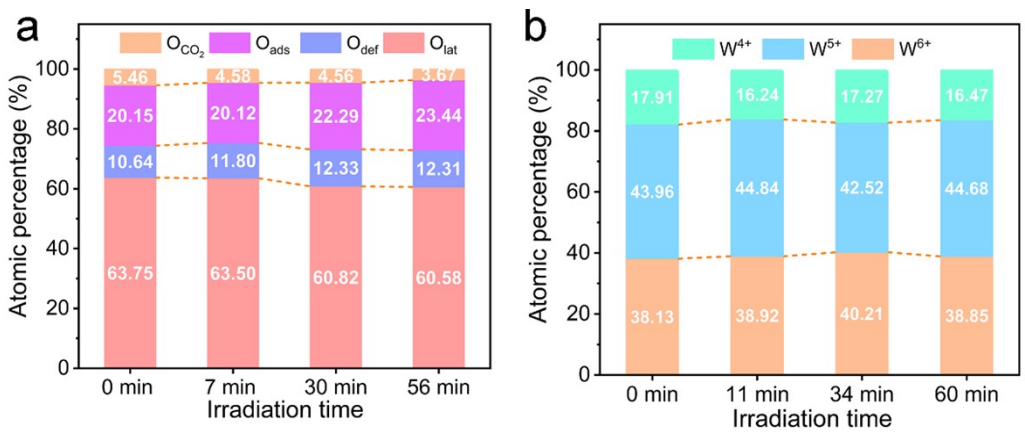

Fig. S16. Atomic proportions of different O and W species calculated from O 1s and W 4f XPS spectra of the preactivated $Pd/W_{18}O_{49}$ catalyst in photocatalytic CO_2 reduction process (1.0 mbar CO_2+H_2O).

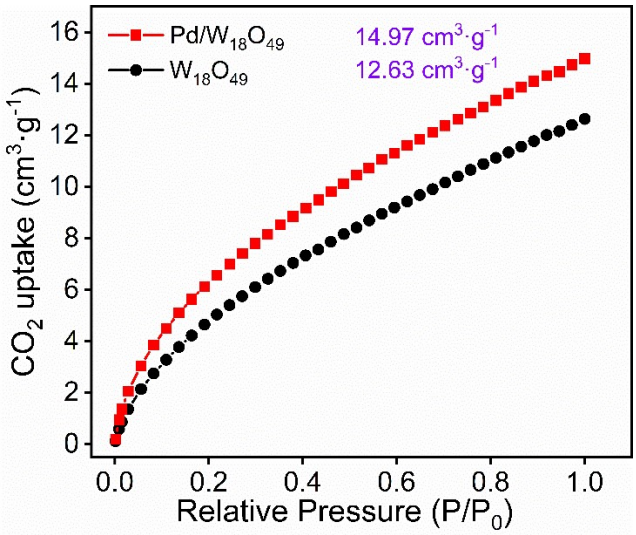

Fig. S17. CO_2 adsorption isotherms of different catalysts measured at 273 K.

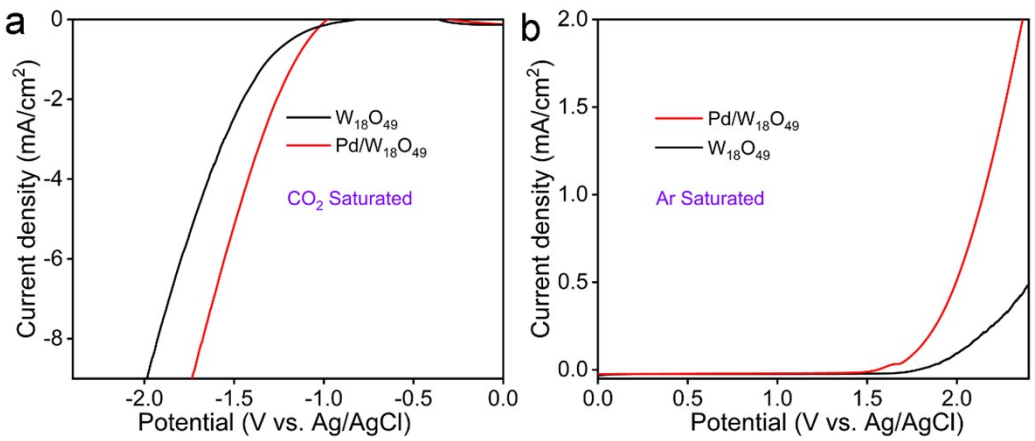

Fig. S18. Linear sweep voltammetry profiles of $W_{18}O_{49}$ and $Pd/W_{18}O_{49}$ coated electrodes measured in (a) CO_2 and (b) Ar-saturated 0.1 M $KHCO_3$ electrolyte.

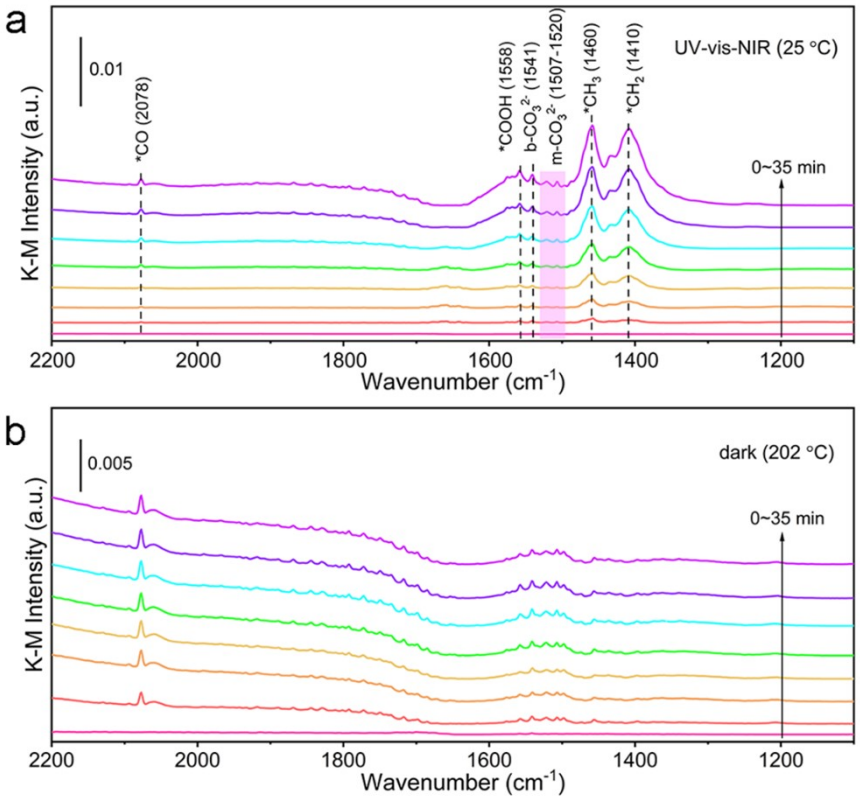

Fig. S19. *In situ* DRIFTS of CO_2 reduction reaction on $Pd/W_{18}O_{49}$ catalyst under different conditions: (a) UV-vis-NIR irradiation at the controlled temperature of 25 °C, (b) without illumination at the controlled temperature of 202 °C.

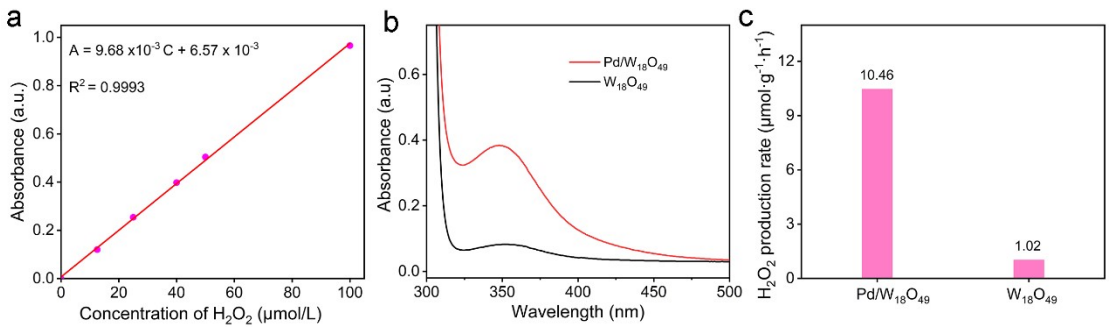

Fig. S20. (a) The standard curve for the quantitative analysis of H_2O_2, (b) UV-vis absorption spectra of the iodometry-testing solutions for detecting H_2O_2 generation in photocatalytic CO_2 reduction with different catalysts. (c) H_2O_2 production rates during photocatalytic CO_2 reduction reaction with different catalysts.

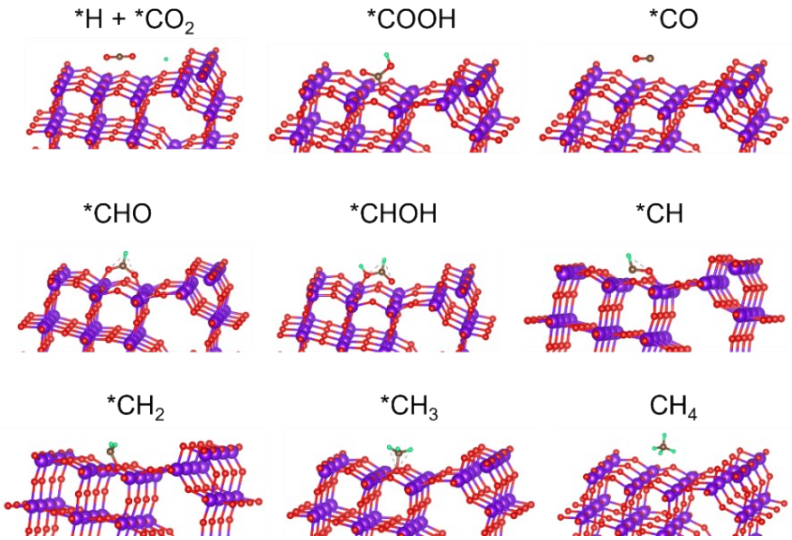

Fig. S21. Optimized structures of the typical intermediates for CO_2 reduction to CH_4 on $W_{18}O_{49}$ with preadsorbed *H.

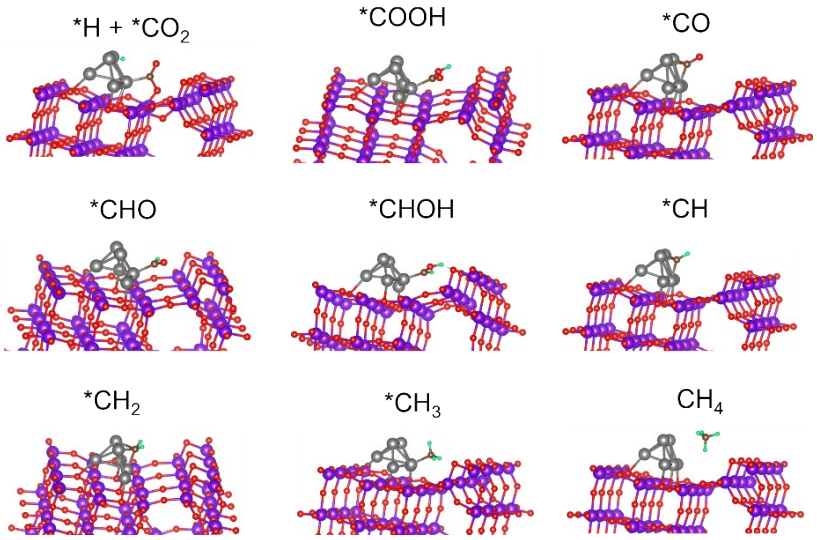

Fig. S22. Optimized structures of the typical intermediates for CO_2 reduction to CH_4 with pre-supplied *H on $Pd/W_{18}O_{49}$.

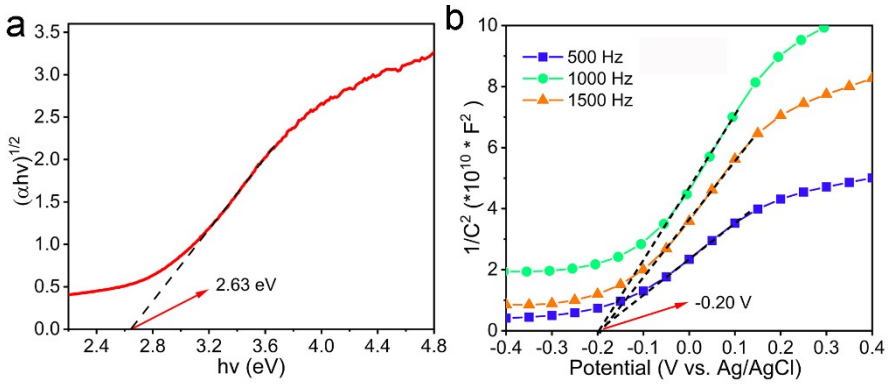

Fig. S23. (a) Tauc plot, and (b) Mott-Schottky plots of the $Pd/W_{18}O_{49}$ catalyst.

The optical bandgap of $W_{18}O_{49}$ in the catalyst can be determined as 2.63 eV. The positive slopes of Mott-Schottky plots indicate that $W_{18}O_{49}$ is an n-type semiconductor. The transverse intercept value of −0.20 V (vs Ag/AgCl, pH = 7) corresponds to the flat-band potential of $W_{18}O_{49}$ in the catalyst, which can be converted to the normal hydrogen electrode (NHE) scale using the following equation: $E_{(NHE)} = E_{(Ag/AgCl)} + 0.197$ V.[1] It is generally considered that the conduction band (CB) position of an n-type

semiconductor is approximately 0.1−0.3 eV below the flat band potential.[1-3] As a result, the CB position is approximate to -0.3 V (vs. NHE), and the VB position is estimated to be 2.33 V (vs. NHE) according to the relationship of $E_g = E_{VBM} - E_{CBM}$.

3. Supplementary Tables

Table S1. BET surface areas and pore size distributions of $W_{18}O_{49}$ and $Pd/W_{18}O_{49}$.

Sample	BET surface area (m^2/g)	Pore volume (cm^3/g)	Average pore size (nm)
$W_{18}O_{49}$	141.694	0.161	4.552
$Pd/W_{18}O_{49}$	126.612	0.135	4.261

Table S2. Atomic proportions of different O and W species from the deconvolution of O 1s and W 4f XPS spectra of the pristine samples.

Sample	O_{lat}	O_{def}	W^{6+}	W^{5+}	W^{4+}
$W_{18}O_{49}$	86.24	13.76	39.28	47.03	13.69
$Pd/W_{18}O_{49}$	92.43	7.57	50.21	40.87	8.92

Table S3. Results of photocatalytic CO_2 reduction reactions under UV-vis illumination in the presence of $W_{18}O_{49}$ and *x*%Pd/$W_{18}O_{49}$ catalysts before and after the preactivation, respectively.

Catalyst	State	CH_4 yield ($\mu mol\ g_{cat}^{-1}\ h^{-1}$)	CO yield ($\mu mol\ g_{cat}^{-1}\ h^{-1}$)	CH_4 yield selectivity (%)
$W_{18}O_{49}$	Pristine	0.57	0.32	64.0
	Preactivated	1.18	0.47	71.5
0.3%Pd/$W_{18}O_{49}$	Pristine	1.78	1.33	57.2
	Preactivated	3.28	1.02	76.3
0.5%Pd/$W_{18}O_{49}$	Pristine	3.26	2.18	59.9
	Preactivated	10.83	1.13	90.6
0.8%Pd/$W_{18}O_{49}$	Pristine	4.39	3.51	55.6
	Preactivated	**12.22**	**1.55**	**88.7**
1.0%Pd/$W_{18}O_{49}$	Pristine	2.62	2.15	54.9
	Preactivated	4.72	1.80	72.4

Table S4. Results of photocatalytic CO_2 reduction reactions under different illuminations in the presence of preactivated Pd/$W_{18}O_{49}$ catalyst.

Entry	Light	Temperature (°C)	CH_4 (μmol g_{cat}^{-1} h^{-1})	CO (μmol g_{cat}^{-1} h^{-1})	CH_4 selectivity (%)
1	UV-vis-NIR	202.7	27.27	1.72	94.1
2	UV-vis	59.9	12.22	1.55	88.7
3	Vis-NIR	180.2	7.28	1.13	86.6
4	Vis	55.0	3.40	0.84	80.2
5	NIR	110.0	3.18	0.89	78.1

Table S5. Cyclic tests of photocatalytic CO_2 reduction on the preactivated Pd/$W_{18}O_{49}$ catalyst under UV-vis-NIR illumination, 5 h for each cycle.

Cycle times	CH_4(μmol g_{cat}^{-1} h^{-1})	CO (μmol g_{cat}^{-1} h^{-1})
1	27.31	1.48
2	26.51	1.43
3	25.51	1.52
4	26.11	1.67

Table S6. The comparison of photocatalytic CO_2 conversion performance between the present $Pd/W_{18}O_{49}$ catalyst and the previously reported $W_{18}O_{49}$-based catalysts.

Catalyst	Reaction system	Photosensitizer & sacrificial agent	Yield rate ($\mu mol\ h^{-1}\ g^{-1}$)	Ref.
$Pd/W_{18}O_{49}$	H_2O vapor + CO_2 gas	/	**CH_4: 27.27** **CO: 1.72**	**This work**
$W_{18}O_{49}$	H_2O + CO_2	/	CH_4: 2.2	4
Cu-$W_{18}O_{49}$	H_2O vapor + CO_2 gas	/	CH_4: 0.67	5
$W_{18}O_{49}$@Co	gas-liquid system	$[Ru(bpy)_3]Cl_2 \cdot 6H_2O$ TEOA	CO: 21.18 H_2: 6.49	2
$Ni_1/WO_{2.72}$	gas-liquid system	$[Ru(bpy)_3]Cl_2 \cdot 6H_2O$ TEOA	CO: 80.5	3
$Au/TiO_2/W_{18}O_{49}$	H_2O vapor + CO_2 gas	/	CH_4: 35.55 CO: 2.57	6
$W_{18}O_{49}/Cu_2O$	H_2O vapor + CO_2 gas	/	CH_4: 17.2	7
SiC-$W_{18}O_{49}$	H_2O vapor + CO_2 gas	/	CH_4: 6.62 CO: 11.96 CH_3OH: 3.29	8
C-$In_2O_3/W_{18}O_{49}$	H_2O+$NaHCO_3$+H_2SO_4	/	CO: 135.82	9

4. References

1 W. Hou, H. Guo, M. Wu and L. Wang, Amide covalent bonding engineering in heterojunction for efficient solar-driven CO_2 reduction, *ACS Nano*, 2023, **17**, 20560-20569.

2 H. Zhang, Y. Wang, S. Zuo, W. Zhou, J. Zhang and X. W. D. Lou, Isolated cobalt centers on $W_{18}O_{49}$ nanowires perform as a reaction switch for efficient CO_2 photoreduction, *J. Am. Chem. Soc.*, 2021, **143**, 2173-2177.

3 Y. Mao, M. Zhang, S. Si, G. Zhai, X. Bao, K. Song, L. Zheng, Y. Liu, Z. Wang, Z. Zheng, P. Wang, Y. Dai, H. Cheng and B. Huang, Electronic structure manipulation via site-selective atomically dispersed Ni for efficient photocatalytic CO_2 reduction, *ACS Catal.*, 2023, **13**, 8362-8371.

4 G. Xi, S. Ouyang, P. Li, J. Ye, Q. Ma, N. Su, H. Bai and C. Wang, Ultrathin $W_{18}O_{49}$ nanowires with diameters below 1 nm: Synthesis, near-infrared absorption, photoluminescence, and photochemical reduction of carbon dioxide, *Angew. Chem. Int. Ed.*, 2012, **51**, 2395-2399.

5 M. Zhang, G. Cheng, Y. Wei, Z. Wen, R. Chen, J. Xiong, W. Li, C. Han and Z. Li, Cuprous ion (Cu^+) doping induced surface/interface engineering for enhancing the CO_2 photoreduction capability of $W_{18}O_{49}$ nanowires, *J. Colloid Interface Sci.*, 2020, **572**, 306-317.

6 X. Jiang, J. Huang, Z. Bi, W. Ni, G. Gurzadyan, Y. Zhu and Z. Zhang, Plasmonic active "hot spots"-confined photocatalytic CO_2 reduction with high selectivity for CH_4 production, *Adv. Mater.*, 2022, **34**, e2109330.

7 M. Jiang, C. Li, K. Huang, Y. Wang, J. H. Liu, Z. Geng, X. Hou, J. Shi and S. Feng, Tuning $W_{18}O_{49}/Cu_2O\{111\}$interfaces for the highly selective CO_2 photocatalytic conversion to CH_4, *ACS Appl. Mater. Interfaces*, 2020, **12**, 35113-35119.

8 M. Lin, M. Luo, Y. Liu, J. Shen, J. Long and Z. Zhang, 1D S-scheme heterojunction of urchin-like SiC-$W_{18}O_{49}$ for enhancing photocatalytic CO_2 reduction, *Chin. J. Catal.* , 2023, **50**, 239-248.

9 H. He, Z. Wang, K. Dai, S. Li and J. Zhang, LSPR-enhanced carbon-coated $In_2O_3/W_{18}O_{49}$ S-scheme heterojunction for efficient CO_2 photoreduction, *Chin. J. Catal.* , 2023, **48**, 267-278.